Original Research

Microcirculatory disturbances and cellular changes during progression of hepatic steatosis to liver tumors

Marie Liebig[1], Alireza Hassanzada[1], Malte Kämmerling[1], Berit Genz[1,2], Brigitte Vollmar[1] and Kerstin Abshagen[1]

[1]Institute for Experimental Surgery, University Medicine Rostock, Rostock 18057, Germany; [2]QIMR Berghofer Medical Research Institute, Brisbane QLD 4006, Australia

Corresponding author: Kerstin Abshagen. Email: kerstin.abshagen@uni-rostock.de

Impact statement

Significant alterations of microcirculation contribute to progression of NAFLD, a chronic liver disease with increasing medical and socio-economic impact. Characterization of microcirculation in a NAFLD model reflecting all relevant stages of disease progression was still missing. Thus, we evaluated microcirculatory and cellular changes in a steatosis-inflammation-tumor model using *in vivo* microscopy. Analyses revealed increasing structural alterations, elevated leukocyte-endothelial interaction, and impaired nutritive perfusion. Thus, this model is suitable for further studies investigating therapeutic approaches targeting these progressive microcirculatory disturbances.

Abstract

Non-alcoholic fatty liver disease is closely associated with metabolic syndrome and comprises a pathological spectrum of liver disease ranging from steatosis to steatohepatitis and can progress to fibrosis/cirrhosis and hepatocellular carcinoma. In 2013, a mouse model was described that mimics non-alcoholic fatty liver disease progression from steatohepatitis to tumors in a short time span and with high incidence. As microcirculatory disturbances play a crucial role in liver disease, the suitability of the steatosis-inflammation-tumor model for microcirculatory studies was assessed. Herein, we present a comprehensive view on morphological, microvascular, cellular, and functional aspects of non-alcoholic fatty liver disease progression in the steatosis-inflammation-tumor model using intravital microscopy, biochemical, and histological techniques. Mice develop steatohepatitis, mild fibrosis, and liver tumors at ages of 6, 12, and 20 weeks, respectively. Non-alcoholic fatty liver disease progression was accompanied by several general aspects of disease severity like increasing liver/body weight index, non-alcoholic fatty liver disease activity score, and hepatocellular apoptosis. Intravital microscopic analysis revealed significant changes in hepatic microcirculation with increasing structural alterations, elevated leukocyte adherence, and impaired nutritive perfusion. Non-alcoholic fatty liver disease was further characterized by a lower sinusoidal density with a striking rise at 20 weeks. The characteristic microcirculatory changes make the model a convenient tool for analysis of microcirculation during progression from steatosis to liver tumor.

Keywords: Non-alcoholic fatty liver disease, steatohepatitis, intravital microscopy, hepatic microcirculation, hepatocellular carcinoma

***Experimental Biology and Medicine* 2018; 243: 1–12. DOI: 10.1177/1535370217738730**

Introduction

Non-alcoholic fatty liver disease (NAFLD), often referred to as the hepatic manifestation of the metabolic syndrome, is a common chronic liver disease[1,2] with growing incidence, particularly in industrialized regions for instance caused by excessive caloric intake. Liver-related conditions are among the leading causes of death worldwide,[3] with liver cancer being the second most common cause of cancer-related deaths.[3]

NAFLD comprises different liver abnormalities extending from simple steatosis in early stages to non-alcoholic steatohepatitis (NASH), which can further progress to end-stage diseases such as cirrhosis and hepatocellular carcinoma (HCC).[4] Usually, patients show no symptoms or non-specific clinical features over a long time period. Thus, diagnosis of NAFLD is often not confirmed before advanced liver injury occurs. Nevertheless, NAFLD can remain non-symptomatic in the form of steatosis or

steatohepatitis without progressing to more severe disease states. Although the theory of the presence of multiple hits has already been proposed, the pathophysiological processes that contribute to the progression of NAFLD are poorly understood.[5,6] Typically, NAFLD and its subsequent conditions are accompanied by obesity and type 2 diabetes mellitus (including hyperinsulinemia, insulin resistance, dyslipidemia, and elevated blood glucose levels).[7]

A wide variety of animal models is used to examine different conditions of the liver. Most of them cover just one or two stages of NAFLD progression and differ in the strategy of disease induction as well as time of disease occurrence. Disease induction can be realized genetically or pharmacologically, by diets or surgical interventions, but only a few models reflect NAFLD progression from early to advanced stages. Additionally, they are often associated with various disadvantages, e.g. a long time span until disease occurrence.[8–10] In 2013, a new animal model (also called "STAM™ mice") was described by Fujii *et al.*[11] These mice showed, in the presence of a fat rich nutrition and elevated blood glucose levels, a liver disease progression from steatosis via NASH and fibrosis to HCC in a comparably short time period of 20 weeks.[11] The mice are exposed to streptozotocin (STZ) two days postnatal, causing hyperglycemia, and are fed a continuous high-fat diet (HFD) from the age of four weeks on, which results in the development of steatosis. To date, this model is used in several studies to investigate NASH pathophysiology and therapeutic approaches,[12–14] liver tumorigenesis, and HCC formation.[15–17] Nevertheless, validation of this model with respect to microcirculatory changes is still lacking.

NAFLD is associated with pathological changes in liver architecture leading to microcirculatory disturbances. Some attempts have already been made to assess the microcirculation in diverse liver diseases. It is known that disease-specific morphological features, e.g. degree of fat accumulation,[18] correlate with the extent of microcirculatory alterations such as sinusoidal endothelial dysfunction, impaired nutritive perfusion, and increased adhesion of leukocytes.[19,20] Additionally, during fibrosis progression sinusoids lose their fenestrae and form a true basement membrane, a process called capillarization.[21,22] In sum, overall changes in microcirculation underlie macroscopically observed changes in NAFLD liver architecture and substantially contribute to disease progression.

The current study aimed to characterize microcirculatory changes in the steatosis-inflammation-tumor model using intravital microscopy. Thus, the applicability of this mouse model for microcirculatory studies of tumor development in steatotic livers was validated.

Materials and methods

Murine steatosis-inflammation-tumor model

The steatosis-inflammation-tumor model was performed as described by Fujii *et al*.[11] The model comprises two independent hits that lead to NAFLD onset and progression. The first hit is an elevated blood glucose level and the second hit comprises a HFD. Hyperglycemia was induced in male C57BL/6 mice (Charles River, Sulzfeld, Germany) through a single intraperitoneal injection of 200 μg STZ (Sigma-Aldrich, St. Louis, Missouri, USA) in 10 μl of 0.05 M trisodium citrate (pH 4.5; Merck, Darmstadt, Germany) at day two postnatal. Starting at day 28 of age, the mice were fed a continuous HFD (fat content: 60 kJ%; D12492 (II) modified experimental diet; Ssniff, Soest, Germany). The mice were kept on water and HFD *ad libitum* at a 12 h light/dark cycle. The general state of health was monitored daily and blood glucose levels and body weight were measured weekly. Additionally, EDTA plasma was collected fortnightly. Animals exhibiting normal blood glucose levels were excluded from the experiment (19 of 151). The ages of 6, 8, 12, and 20 weeks served as final observation time points. For each time point, a set of mice was used for intravital microscopic analysis (n=8–11 per time point). Additionally, mice were sacrificed at the named time points (n=7–9 per time point). EDTA plasma was collected and the liver was excised and weighed. For histological analyses, the left lateral liver lobe was fixed in formalin and half of the medial liver lobe was embedded in Tissue-Tek® (Sakura, Tokyo, Japan), subsequently snap frozen in liquid nitrogen, and stored at −20°C. The remaining liver tissue was snap frozen in liquid nitrogen and stored at −80°C. Healthy C57BL/6 mice without STZ treatment and HFD served as control mice. All animal experiments were approved by "Landesamt für Landwirtschaft, Lebensmittelsicherheit und Fischerei Mecklenburg-Vorpommern" (7221.3-1-039/14) and were executed in accordance with the German legislation and EU-directive 2010/63/EU.

In vivo microscopy and quantitative off-line analysis

At ages of 6, 8, 12, and 20 weeks, respectively, *in vivo* microscopy of the liver was performed and analyzed as described previously by our group.[23–25] Under ketamine/xylazine anesthesia (90/7 mg/kg body weight ip) mice were laparotomized, the left lateral liver lobe was exteriorized on a plasticine stage and covered with a glass coverslip. *In vivo* microscopy with ultraviolet epi-illumination was used to examine hepatic stellate cells (HSCs) by vitamin A autofluorescence. Thereafter, sodium fluorescein (2 μmol/kg), rhodamine 6G (1 μmol/kg), and bisbenzimide (10 μmol/kg) were injected via the vena jugularis. Sodium fluorescein fluorescence was assessed using blue light epi-illumination. Through enhancement of tissue contrast vessel diameter, blood velocity, sinusoidal density, and sinusoidal perfusion were analyzed. Direct staining of leukocytes by rhodamine 6G facilitated analysis of venular leukocyte rolling and adherence, and sinusoidal leukocyte stasis using green light epi-illumination. Apoptotic cell death was analyzed by means of ultraviolet epi-illumination and bisbenzimide staining of hepatocellular nuclei. A computer-assisted image analysis system (CapImage, Zeintl, Heidelberg, Germany) was used for quantitative off-line analysis of the video files. Volumetric blood flow VQ (sinusoidal and venular, equation (1)) and shear stress τ (sinusoidal and venular, equation (2)) were

calculated from blood velocity (vRBC) and vessel radius (r) as below.

$$VQ = vRBC * \pi * r^2 \quad (1)$$

$$\tau = \frac{4 * n * VQ}{\pi * r^3} \quad (2)$$

Hematological measurements and plasma analyses

Alanine aminotransferase (ALT) and glutamate dehydrogenase (GLDH) activities in EDTA plasma were determined spectrophotometrically using cobas c 111 analyzer (Roche Diagnostics; Rotkreuz, Switzerland) according to the manufacturer's instructions. Blood glucose levels were measured using a Contour blood glucose meter (Bayer Vital, Leverkusen, Germany) with one drop of blood from the tail vein. For analysis of plasma triglyceride levels, a triglyceride colorimetric assay kit (Cayman Chemical Company, MI, USA; 10010303) was used according to manufacturer's instructions. Malondialdehyde (MDA) in plasma was measured using the MDA-586-method according to manufacturer's instructions (OxisResearchTM, Portland, OR). For assessment of non-fasting plasma insulin concentration, the ultra-sensitive mouse insulin ELISA (Crystal Chem, Zaandam, Netherlands) was conducted according to manufacturer's instructions.

Histology, immunohistochemistry, and image analysis

Liver tissue was fixed in 4% phosphate-buffered formalin (Grimm med. Logistik, Torgelow, Germany) for two to three days, embedded in paraffin, and cut into 5 µm thick sections. Assessment of all histological stainings was performed in a blinded manner. Hematoxylin and eosin (H&E) staining was used to determine NAFLD activity score (NAS). The total NAS (score 0–8) was calculated as the sum of three different scores, namely steatosis (score 0–3), lobular inflammation (score 0–3), and hepatocellular ballooning (score 0–2).[26] For scoring of lobular inflammation, we defined an inflammatory focus as a group of at least five inflammatory cells that were not aligned in a row. All scores were determined by three to four independent observers in a blinded manner.

For additional assessment of inflammatory processes, namely tissue infiltration of granulocytes, sectioned paraffin-embedded liver tissue was stained for CAE (chloracetate esterase) with Naphthol AS-D chloroacetate (Sigma-Aldrich, St. Louis, Missouri, USA) and counterstained with hematoxylin (Merck, Darmstadt, Germany). For quantification, CAE positive cells were counted in 30 consecutive high-power fields (HPFs).

For Oil Red O staining of lipids, the liver tissue was embedded in Tissue-Tek®, snap frozen in liquid nitrogen, and stored at −20°C. The tissue was cut in 8 µm thick sections, air dried, and fixed in paraformaldehyde (ChemCruz, Dallas, TX). The staining was performed using Oil Red O (Sigma-Aldrich, St. Louis, Missouri) and counterstained with hematoxylin. Ten to 20 photographs were taken per sample in a 200× magnification. Quantitative analysis of the red stained area was conducted using Adobe Photoshop CS5 analyzing the percentage of red pixels per image.

Liver cell death was detected by ApopTag® plus peroxidase in situ apoptosis kit (Merck, Darmstadt, Germany) according to the manufacturer's instructions. For quantitative analysis, positive cells were counted in 14 consecutive HPFs.

To assess fibrosis, immunohistochemical staining of collagen 1α in liver sections was performed as follows: Paraffin sections were incubated at 4°C overnight with a primary antibody against collagen 1α (ab34710; Abcam, Cambridge, UK) and subsequently incubated with a horseradish peroxidase-(HRP) conjugated secondary antibody (P0448; Dako, Hamburg, Germany) at room temperature for 1 h. The antibody signals were detected with 3,3′-Diaminobenzidine (Dako, Hamburg, Germany) followed by counterstaining with hematoxylin. For quantitative analysis of the staining, 10 to 20 photographs in a 200× magnification were taken per object. The positive stained area was analyzed as the percentage of brown pixels per image with Adobe Photoshop CS5.

Liver macrophages were stained immunohistochemically with F4/80 specific antibody (MCA-497, 1:10, Serotec, Oxford, UK) and matching secondary antibody (sc-2021, 1:200, Santa-Cruz) as described previously by our group.[27]

Western blot

Snap-frozen liver tissue was homogenized, lysed in lysis buffer (50 mM Tris-HCl, 150 mM NaCl, 1% NP-40, 0.5% sodium deoxycholate, 0.1% SDS, 10× protease inhibitor) for 30 min on ice and centrifuged for 10 min at 10,000 × *g*. The concentration of extracted protein was determined using Pierce BCA protein assay kit (Thermo Fisher Scientific, Waltham, Massachusetts) with BSA serving as a standard. SDS gel electrophoresis was conducted with 40 µg extracted protein per lane on a 12% SDS gel. The separated proteins were transferred to nitrocellulose membranes (Amersham Biosciences, Freiburg, Germany) and stained for α smooth muscle actin (αSMA) and GAPDH. Primary antibodies against αSMA (1:1.000, A2547, Sigma-Aldrich, St. Louis, Missouri) and GAPDH (1:20.000, MAB374, Merck Millipore, Darmstadt, Germany) were incubated overnight at 4°C in 2.5% BSA. An antibody conjugated to HRP was used as secondary antibody (1:20.000 for αSMA and 1:40.000 for GAPDH, A9044, Sigma-Aldrich, St. Louis, Missouri; 1 h room temperature) and was detected using ECL Western blot reagents (Amersham Biosciences, Amersham, UK). The signals were quantitatively analyzed with Quantitiy One 1D analysis software (Bio-Rad, Hercules, California) and αSMA signals were normalized to GAPDH signals.

Statistical analysis

Data are presented as mean±s.e.m. if normally distributed and as median if not normally distributed. In normally distributed data sets with more than nine data points, outliers were identified using Grubb's test and were excluded if significance was $p<0.05$. Statistical analysis was performed using Sigma-Plot 12.0 (Systat Software Inc., Erkrath, Germany).

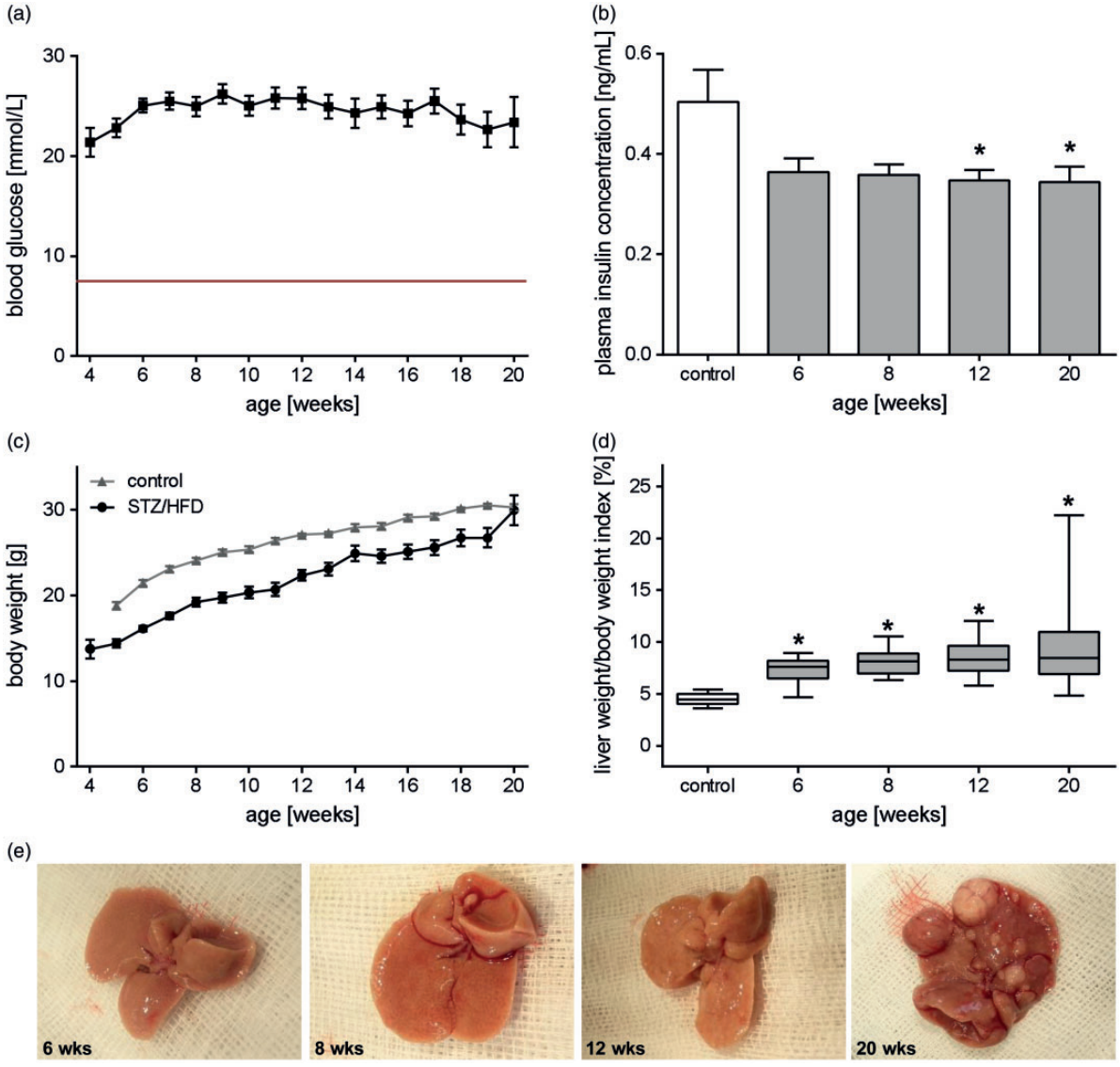

Figure 1. General characteristics during progression of NAFLD. (a) Non-fasting blood glucose levels of all analyzed STZ/HFD-treated mice at the ages from 4 to 20 weeks given as mean±s.e.m. (n=12–74). The red line represents the mean blood glucose value of healthy mice. (b) Non-fasting plasma insulin concentration of untreated (control) and STZ/HFD-treated mice. Values are given as mean±s.e.m. (control: n=4, 6 weeks: n=5, 8 weeks: n=5, 12 weeks: n=5, 20 weeks: n=6). Significance of differences between the groups was tested by one-way ANOVA (Holm-Sidak method), *$P<0.05$ vs. control. (c) Body weight of all analyzed STZ/HFD-treated mice at the ages from 4 to 20 weeks compared to healthy controls given as mean±s.e.m. (n=12–74). (d) Calculation of the liver to body weight ratio. Data (control: n=13, 6 weeks: n=17, 8 weeks: n=17, 12 weeks: n=19, 20 weeks: n=23) are presented as box plots indicating the median, the interquartile range in form of a box, and the minimum and maximum as whiskers. Significance of differences between the groups was tested by one-way ANOVA on Ranks (Kruskal–Wallis); *$P<0.05$ versus control. (e) Macroscopic images of livers of mice treated with STZ/HFD at an age of 6, 8, 12, and 20 weeks. (A color version of this figure is available in the online journal.)

After testing for normality and equal variance across groups, differences between the groups were assessed by one-way ANOVA, followed by the appropriate *post hoc* comparison test. If the data were not normally distributed, one-way ANOVA on Ranks was performed. Statistical significance was set at $p<0.05$. For details see figure legends.

Results

General aspects

Treatment of mice with STZ led to increased blood glucose levels throughout the entire observation period with blood glucose levels of about 20 mmol/L (Figure 1(a)). Elevated blood glucose levels were accompanied by slightly (at 12 and 20 weeks significantly) reduced non-fasting plasma insulin levels compared to healthy mice (Figure 1(b)). Feeding of a HFD resulted in continuously elevated plasma triglyceride levels (data not shown). Body weight of STZ/HFD-treated mice increased slowly over the period of 20 weeks (wks), but was generally 10–20% lower when compared to healthy mice of the same age (Figure 1(c)). However, liver weight increased disproportionately compared to body weight, leading to a continuously increasing liver/body weight index over time (Figure 1(d) and (e)). This model was associated with a mortality rate of about 28% (37 of 132) over the period of 20 weeks.

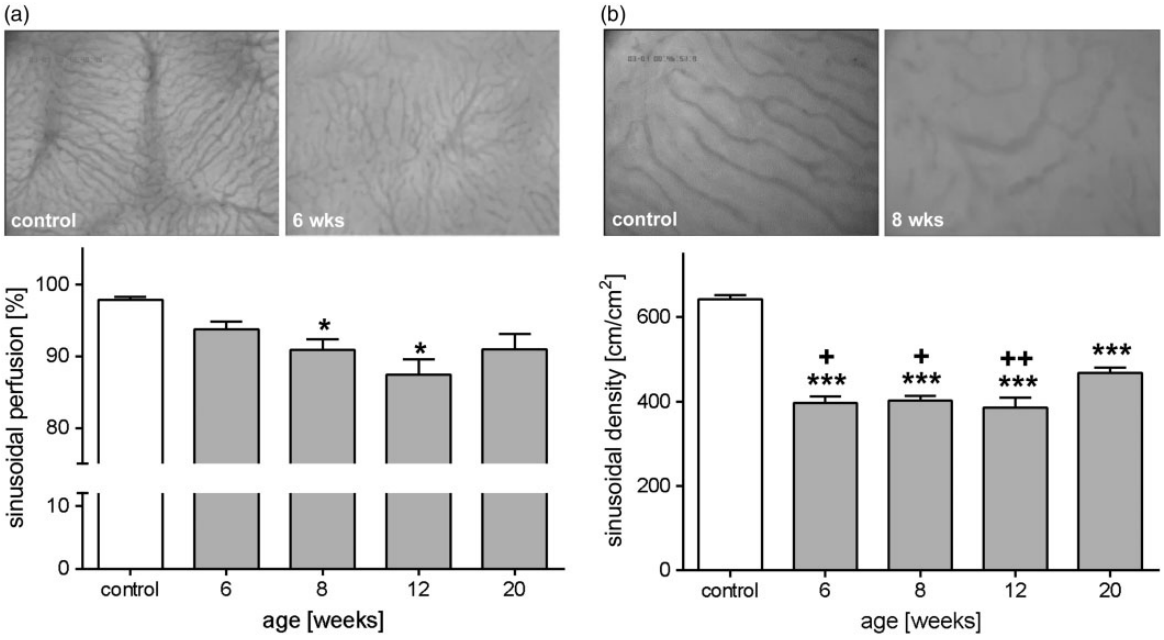

Figure 2. Impaired nutritive perfusion in NAFLD. Quantitative *in vivo* microscopic analysis of sinusoidal perfusion (a) and density (b) of control mice and mice treated with STZ/HFD at ages of 6, 8, 12, and 20 weeks. (a) Percentage of perfused sinusoids (control: n=10, 6 weeks: n=11, 8 weeks: n=10, 12 weeks: n=10, 20 weeks: n=11) and appropriate representative images (200× magnification) for control and six weeks old STZ/HFD-treated mouse showing decreased nutritive perfusion and tortuous sinusoids. Values are given as mean±s.e.m. (b) Quantification of sinusoidal length per area regardless of perfusion. Values are given as mean±s.e.m. (control: n=10, 6 weeks: n=10, 8 weeks: n=10, 12 weeks: n=10, 20 weeks: n=10). Depicted are representative images (400× magnification) of a control mouse and a eight weeks old mouse treated with STZ/HFD. Significance of differences between the groups was tested by one-way ANOVA (Holm-Sidak method; sinusoidal length per area) and one-way ANOVA on Ranks (Kruskal–Wallis; perfused sinusoids), $^{*}P<0.05$ vs. control; $^{***}P<0.001$ vs. control; $^{+}P<0.05$ vs. 20 wks; $^{+++}P<0.01$ vs. 20 weeks.

Hepatic microcirculation and microhemodynamics

Microcirculatory changes during NAFLD progression were examined by means of *in vivo* fluorescence microscopy. Hepatic microvasculature in STZ/HFD-treated mice was characterized by an impairment of nutritive perfusion with a high number of non-perfused sinusoids. This resulted in a reduced sinusoidal perfusion rate at all examined time points, with 8 and 12 weeks being significantly diminished by 7% and 11%, compared to healthy mice (Figure 2(a)). Simultaneously, morphological density of sinusoids was significantly reduced at all time points compared to control mice (Figure 2(b)). Further analysis even showed lipid-laden hepatocytes, resulting in tortuous appearance of sinusoids varying from small to large diameters. Nevertheless, slightly increasing sinusoidal diameters were observed over time (Table 1). In contrast, the venular diameters were marginally reduced at six weeks (Table 1). In correlation with disease severity, normal vascular architecture was more and more lost and changed to an irregular and distorted sinusoidal network (Figure 2). Particularly for the tumor state (20 weeks), numerous superficial vessels and highly vascularized zones were striking, which resulted in an overall higher sinusoidal density compared to the other disease stages (Figure 2 (b)). Quantitative analysis of hepatic microhemodynamics revealed no significant changes of venular and sinusoidal blood velocity in STZ/HFD-treated mice compared to control animals. Consequently, volumetric blood flow in venules and sinusoids was found to be almost unchanged. Calculation of the shear stress revealed marginally reduced values in venules and sinusoids at late time points (Table 1).

Steatosis

Fat deposition in the liver was assessed by quantitative analysis of Oil Red O-stained frozen liver sections. While healthy animals revealed lipid contents of about 8% (red line), Oil Red O positive area of the liver in STZ/HFD-treated mice was markedly increased at all time points, reaching values of 20–30% (Figure 3(a)). Oil Red O (Figure 3(a)) but also H&E staining (Figure 6(e)) showed both micro- and macrovesicular steatosis being present independent of the time point. Particularly in livers of 20 weeks old mice, in accordance with tumor development, fat was rather heterogeneously distributed. As lipid peroxidation is used as an indicator of oxidative stress, the lipid peroxide MDA was measured systemically (Figure 3(b)). Compared to healthy animals, plasma MDA levels were significantly elevated during almost the entire observation period of 20 weeks.

Inflammation

In vivo fluorescence microscopic analysis of leukocyte interaction with the microvascular endothelium revealed massively and significantly increased leukocyte adherence in postsinusoidal venules at all time points of STZ/HFD-treated mice compared to control mice (Figure 4(a) and (c)). This observation was accompanied by continuously

Table 1. Microhemodynamic parameters analyzed by *in vivo* microscopy.

	Control	6 weeks	8 weeks	12 weeks	20 weeks
Sinusoidal vRBC (μm/s)	147.3 (96.7/203.5)	148.4 (129.6/224.7)	152.5 (108.0/236.5)	121.0 (95.9/223.5)	127.6 (90.0/225.6)
Venular vRBC (μm/s)	268.2 ± 19.0	227.1 ± 12.8	242.7 ± 16.4	228.6 ± 12.3	228.2 ± 14.6
Sinusoidal diameter (μm)	6.7 ± 0.2	6.7 ± 0.1*	7.2 ± 0.2	7.3 ± 0.2	7.5 ± 0.2
Venular diameter (μm)	23.6 ± 2.7	18.0 ± 1.6	20.2 ± 0.9	27.0 ± 2.9	26.0 ± 2.3
Sinusoidal volumetric blood flow (pL/s)	5.5 ± 0.5	5.4 ± 0.3	6.7 ± 0.6	5.0 ± 0.4	5.9 ± 0.4
Venular volumetric blood flow (pL/s)	98.2 (29.4/460.5)	72.5 (13.7/105.3)	94.8 (46.8/130.3)	137.7 (32.7/583.7)	124.0 (44.5/326.9)
Sinusoidal shear stress (dyn/cm^2)	17.9 (12.3/25.7)	18.3 (15.5/19.8)	16.1 (11.9/29.9)	13.4 (9.8/23.5)	12.9 (8.8/26.5)
Venular shear stress (dyn/cm^2)	10.9 (6.7/14.0)	10.2 (7.4/22.8)	10.4 (7.1/15.6)	7.7 (4.8/10.7)	8.0 (3.9/13.9)

Note: Namely, red blood cell velocity (vRBC), vessel diameter, volumetric blood flow, and shear stress were measured in sinusoids as well as postsinusoidal venules. The values are given as mean±s.e.m. if normally distributed and median with minimum/maximum if not normally distributed (n=8–11 per time point). Significance of differences between the groups was tested by one-way ANOVA (Dunn's method; sinusoidal diameter).
*$P<0.05$ vs. 20 weeks.

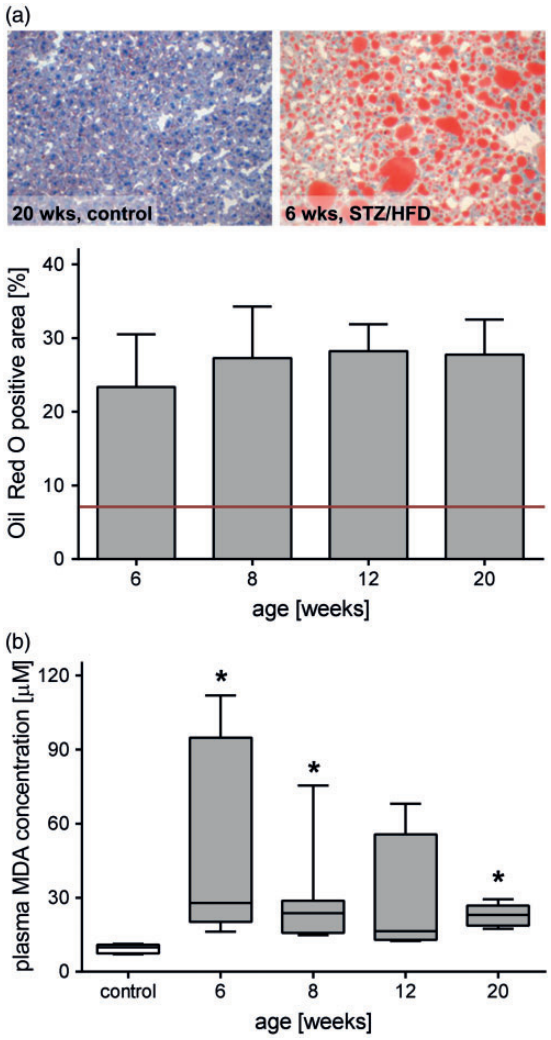

Figure 3. Raised hepatic lipid content and systemic lipid peroxidation in NAFLD. (a) Quantitative analysis of lipids by Oil Red O staining in livers of 6, 8, 12, and 20 weeks old mice treated with STZ/HFD and appropriate representative images of Oil Red O stained liver sections. Values are given as mean±s.e.m. (6 wks: n=7, 8 wks: n=7, 12 wks: n=6, 20 wks: n=7). The red line indicates basal level of hepatic fat content in healthy mice (~8%). (b) Quantitative measurement of malondialdehyd (MDA) in plasma as a biomarker of lipid peroxidation. Values are given as mean±s.e.m. (control: n=7, 6 weeks: n=7, 8 weeks: n=7, 12 weeks: n=4, 20 weeks: n=6). Significance of differences between the groups was tested by one-way ANOVA on Ranks (Kruskal–Wallis); *$P<0.05$ vs. control. (A color version of this figure is available in the online journal.)

increasing sinusoidal leukostasis (Figure 4(d)). Elevated adherence of leukocytes in venules leads to leukocyte migration into the liver parenchyma and thus reflects ongoing inflammatory processes. To further investigate inflammation, the number of granulocytes in the liver tissue was histologically assessed by quantitative analysis of CAE staining (Figure 4(b) and (c)). During NAFLD progression, numbers of infiltrated granulocytes increased, reaching a peak at 12 weeks (Figure 4(b) and (c)). At the same time, the number of F4/80-stained cells, namely Kupffer cells and monocyte derived macrophages, remained unchanged during NAFLD progression (data not shown).

Fibrosis/end-stage liver disease

Steatohepatitis is continuously challenging the liver tissue which in turn can lead to remodeling of extracellular matrix and fibrosis. HSCs play a crucial role in fibrosis development. HSCs exhibit a transition from a quiescent to a proliferative fibroblast-like phenotype that is accompanied by loss of intracellular vitamin A. Evaluation of vitamin A-positive spots by means of IVM revealed a decreased number in STZ/HFD-treated mice at all time points compared to healthy animals, being significantly reduced at eight weeks (Figure 5(a)). Concomitantly, activation of HSCs is characterized by increased expression of αSMA. Indeed, we observed elevated αSMA protein expression in STZ/HFD-treated mice, particularly at an age of 12 weeks (Figure 5(b)). Consequently, HSC activation leads to increased collagen 1α deposition. Quantitative assessment of collagen 1α via immunohistochemical staining revealed highest collagen 1α content of about 17% at 12 weeks of age, being significantly increased compared to 8 weeks (Figure 5(c)). The observed slight reduction of fibrotic markers (collagen 1α deposition and αSMA expression) at 20 weeks was explained by the highly heterogeneous appearance of livers at this time point with tumors often being non-fibrotic. Chronic hyperglycemia and HFD induced tissue damage and functional impairment of the liver. Initially, plasma activities of ALT and GLDH were only slightly elevated, but increased continuously with severity of the liver disease (Figure 6(a)). In accordance with that observation, *in vivo* analysis of bisbenzimide-stained hepatocytes unveiled elevated numbers of

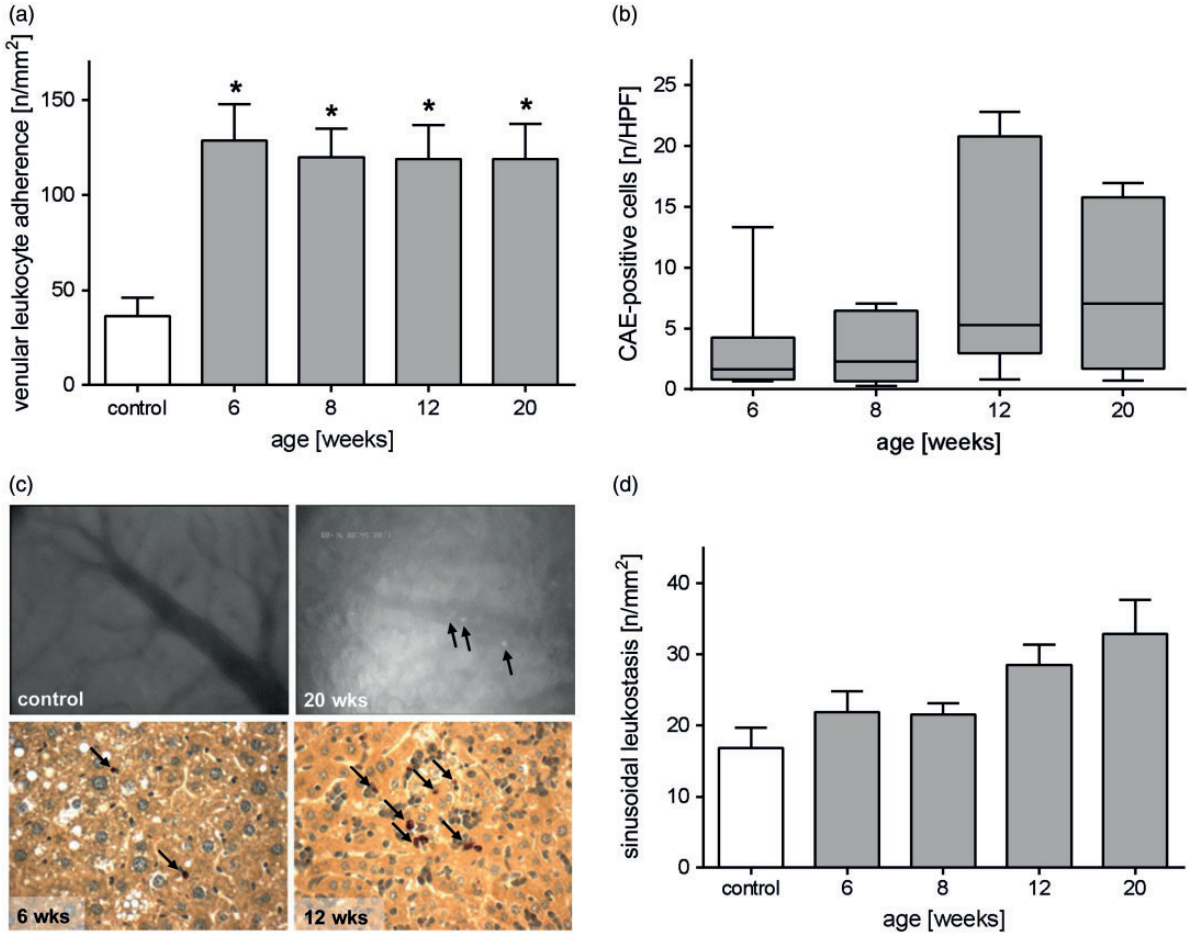

Figure 4. Increased hepatic inflammation during progression of NAFLD. (a) Intravital microscopic analysis of the number of adherent leukocytes in postsinusoidal venules of healthy livers (control) and livers of STZ/HFD-treated mice at ages of 6, 8, 12, and 20 weeks. Values are given as mean±s.e.m. (control: n=9, 6 weeks: n=10, 8 weeks: n=10, 12 weeks: n=10, 20 weeks: n=11). Significance of differences between the groups was tested by one-way ANOVA (Bonferroni t-test), $^*P<0.05$ vs. control. (b) Quantitative analysis of CAE-positive cells in liver sections of STZ/HFD-treated mice (6, 8, 12, and 20 weeks). Data are presented as box plots indicating the median, the interquartile range in form of a box, and the minimum and maximum as whiskers (6 weeks: n=7, 8 weeks: n=7, 12 weeks: n=9, 20 weeks: n=7). (c) Upper panel: Representative *in vivo* images of the liver of a control and a 20 weeks old STZ/HFD-treated mouse showing numerous leukocytes (arrows) adhering at the endothelium of the venule in the diseased liver (12 weeks) (400× magnification). Lower panel: The images depict representative HPF of CAE-stained liver tissue of 6 and 12 weeks old mice with red stained granulocytes (arrows). (d) Intravital microscopic analysis of sinusoidal leukostasis of healthy livers (control) and livers of STZ/HFD-treated mice at ages of 6, 8, 12, and 20 weeks. Values are given as mean±s.e.m. (control: n=11, 6 weeks: n=10, 8 weeks: n=10, 12 weeks: n=10, 20 weeks: n=10). (A color version of this figure is available in the online journal.)

apoptotic cells at all observed time points, with 20 weeks being significantly increased compared to untreated mice (Figure 6(c)). This was also verified by immunohistochemical assessment of cell death in TdT-mediated dUTP-biotin nick end labeling (TUNEL)-stained liver sections (Figure 6 (d)). Even though that NAFLD activity score is not suitable for tumor assessment, it differentiates NAFLD severity grades and progression stages. In STZ/HFD-treated mice, NAS increased with age and disease severity, confirming progression of NAFLD (Figure 6(b)). At late time points, different types of tumors were observed, reaching from neoplasia with high-fat content but intact vascular architecture, unstructured tumors displaying a loss of vascular architecture, to highly differentiated HCC of pseudoglandular and trabecular type (Figure 6(e)). While no tumors were observed at the time points 6 and 8 weeks, 41% of 12 weeks old (n=17) and 84% of 20 weeks old mice (n=19) displayed tumors (Figure 1(e)).

Discussion

NAFLD is becoming an increasingly important risk factor for the development of end-stage liver disease.[28] Simple steatosis of the liver can proceed to steatohepatitis, fibrosis, cirrhosis, and finally HCC. As microcirculatory changes are present in this progression, their investigation is fundamental for deeper understanding of the underlying pathophysiological mechanisms and thus for development of innovative therapeutics against NAFLD progression. A broad variety of experimental mouse models exist that mimic NAFLD, its progression, or HCC development. Still, well described models are missing that represent progression from steatosis to tumors in a short time period and with high incidence. The steatosis-inflammation-tumor model used in this study was first described by Fujii *et al.*[11] and features NAFLD progression from steatosis to fibrosis and tumor formation within only 20 weeks, making

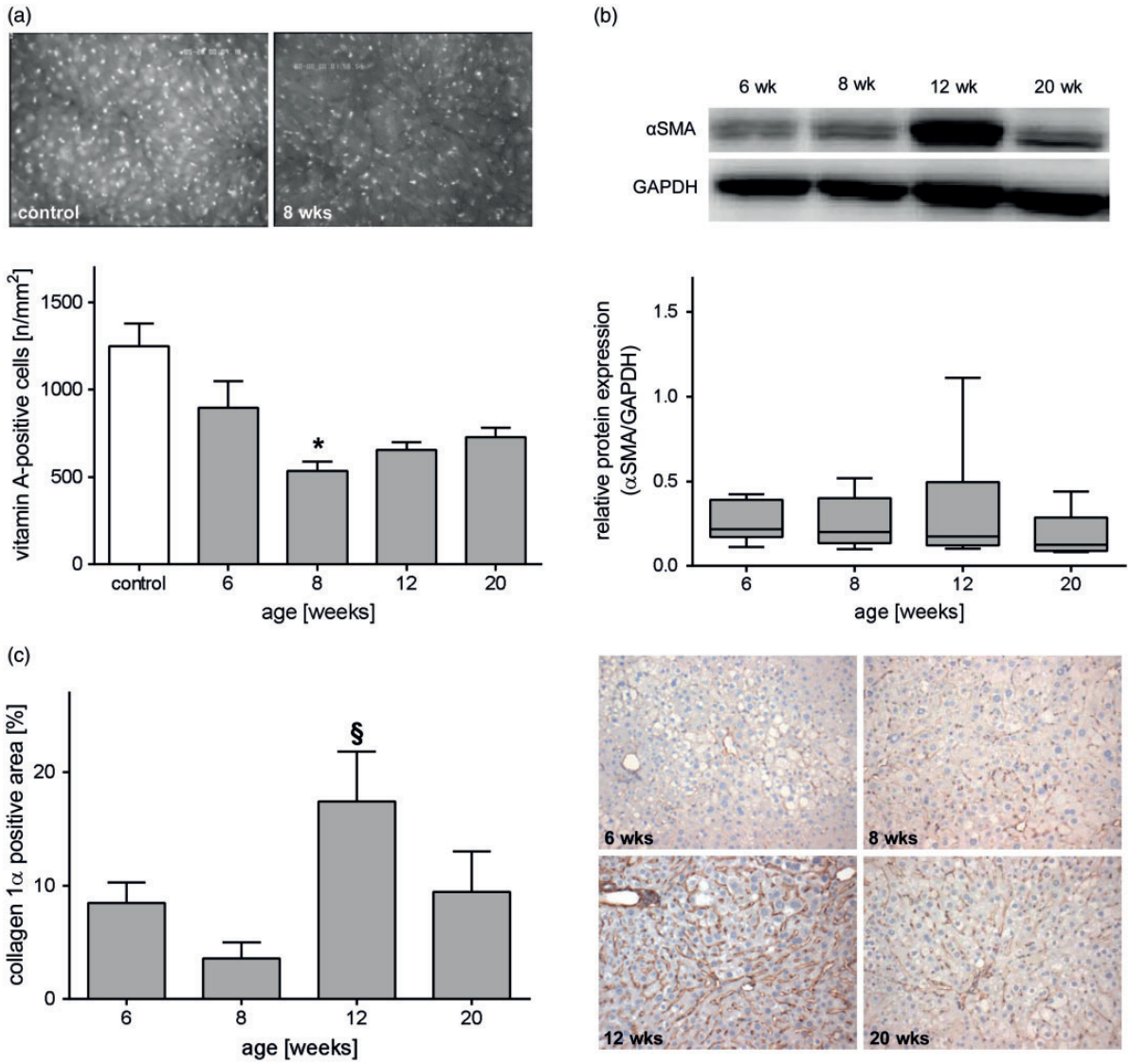

Figure 5. Analysis of hepatic stellate cell activation. Quantitative analysis of hepatic stellate cells by means of (a) IVM, (b) αSMA Western blot, and (c) collagen 1α staining. (a) *In vivo* quantification of vitamin A-positive cells of control mice and STZ/HFD treated mice at ages of 6, 8, 12, and 20 weeks. Depicted are representative images (200× magnification) of a healthy mouse and an eight weeks old mouse treated with STZ/HFD showing the decrease in vitamin A autofluorescent spots during NAFLD progression. Values are given as mean±s.e.m. (control: n=10, 6 weeks: n=11, 8 weeks: n=10, 12 weeks: n=10, 20 weeks: n=12). Significance of differences between the groups was tested by one-way ANOVA on Ranks (Kruskal–Wallis), $^{*}P<0.05$ vs. control. (b) Quantitative analysis of hepatic protein expression of αSMA relative to GAPDH protein expression of STZ/HFD-treated mice at an age of 6, 8, 12, and 20 weeks. Data are presented as box plots indicating the median, the interquartile range in form of a box, and the minimum and maximum as whiskers (6 weeks: **n**=7, 8 weeks: n=7, 12 weeks: n=9, 20 weeks: n=7). (c) Quantitative analysis of collagen 1α-staining in livers of 6, 8, 12, and 20 weeks old mice treated with STZ/HFD and representative images of collagen 1α immunohistochemistry (200× magnification). Values are given as mean±s.e.m. (6 weeks: n=7, 8 weeks: n=7, 12 weeks: n=8, 20 weeks: n=7). Significance of differences between the groups was tested by one-way ANOVA (Holm-Sidak), $^{§}P<0.05$ vs. eight weeks. (A color version of this figure is available in the online journal.)

it a good model for development of novel drug interventions and investigation of tumor formation. While analyses of microhemodynamics of fatty livers have already been performed by numerous groups,[29–32] no comparative study specified the progression to liver cancer. Using intravital microscopy, we characterized progressive changes of hepatic microcirculation and microhemodynamics in the steatosis-inflammation-tumor model.

Infiltration of immune cells into the liver parenchyma is one of the hallmarks in steatohepatitis and NAFLD progression. Beside resident liver cells, invading monocyte-derived macrophages, neutrophils, eosinophils, and lymphocytes comprise the mixed inflammatory cell infiltrate in NASH.[33,34] In line with this, we observed constantly high venular leukocyte adherence and increasing sinusoidal leukostasis during progression of NAFLD which was in part reported in other *in vivo* models of NAFLD.[31,32] Adhered to venules and sinusoids, leukocytes can infiltrate hepatic parenchyma by endothelial cell interaction.[35] VCAM-1 and ICAM play essential roles during adherence[35] and are up-regulated by the NF-kB signaling pathway.[36] NF-kB in turn is known to be activated as a response to oxidative stress.[37] Accordingly, we observed increased levels of MDA in plasma pointing towards increased

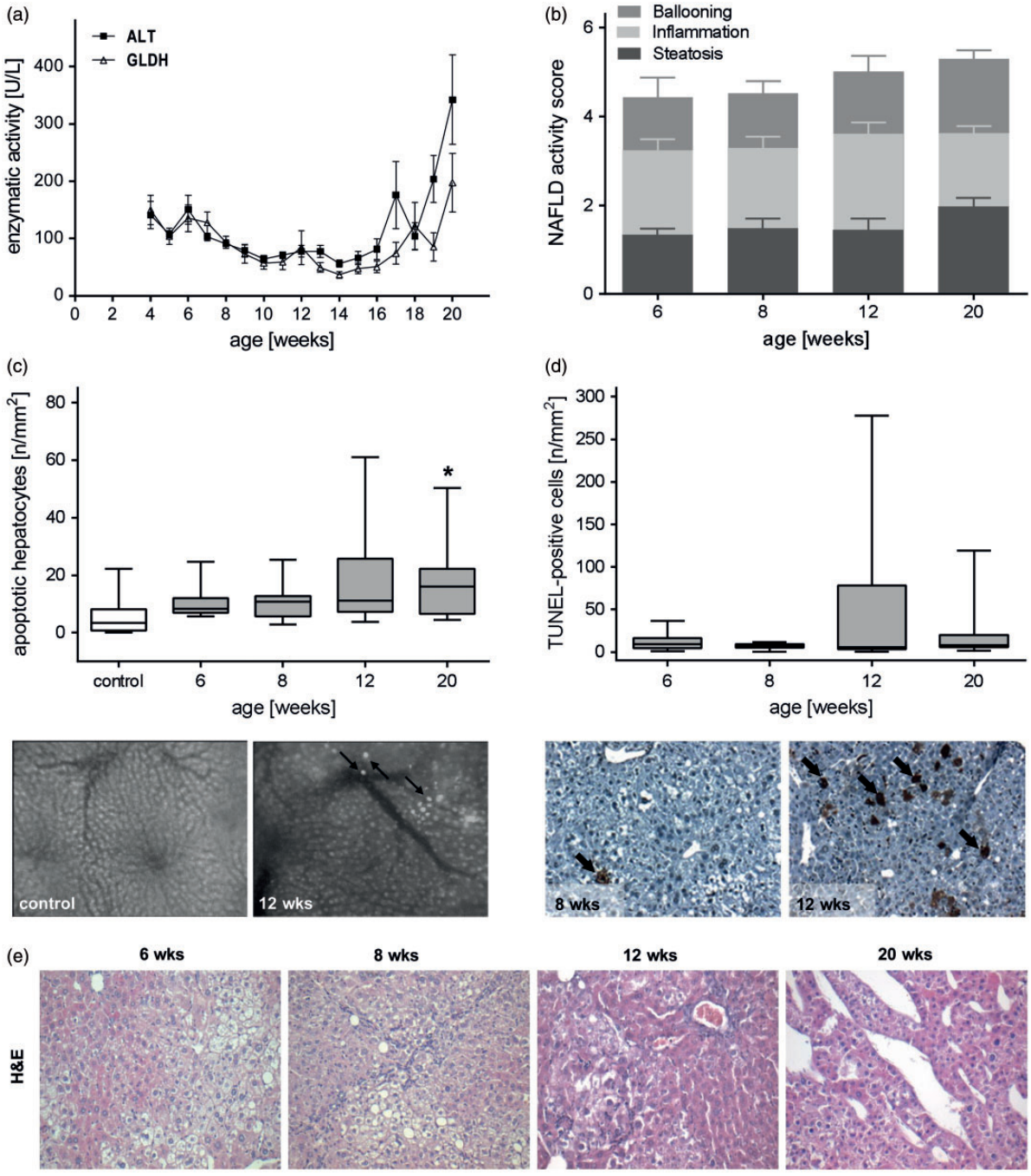

Figure 6. Progression of liver injury during NAFLD. (a) ALT and GLDH activities in plasma of all analyzed STZ/HFD-treated mice at the ages from 4 to 20 weeks given as mean±s.e.m. (n=6–26). (b) NAFLD activity score including subscores (ballooning, inflammation and steatosis) of STZ/HFD treated mice given as mean±s.e.m. (6 weeks: n=7, 8 weeks: n=7, 12 weeks: n=9, 20 weeks: n=7). (c) *In vivo* analysis of apoptotic hepatocytes in control and STZ/HFD treated mice by means of IVM and representative *in vivo* images (200× magnification) of a control liver and a liver of a STZ/HFD treated (12 weeks) mouse displaying apoptotic hepatocytes (arrows) appearing as bright spots due to chromatin condensation. Data are presented as box plots indicating the median, the interquartile range in form of a box, and the minimum and maximum as whiskers (control: n=10, 6 weeks: n=11, 8 weeks: n=10, 12 weeks: n=10, 20 weeks: n=11). Significance of differences between the groups was tested by one-way ANOVA on Ranks (Kruskal–Wallis), *$P<0.05$ vs. control. (d) Quantitative immunohistochemical analysis of TUNEL-positive cells (arrows) and representative images of TUNEL-stained liver sections (200× magnification). Data are presented as box plots indicating the median, the interquartile range in form of a box, and the minimum and maximum as whiskers (n=7 per group). In healthy animals, almost no TUNEL-positive cells are present.[23] (e) Representative images of H&E-stained liver sections of HFD/STZ-treated mice at ages of 6, 8, 12, and 20 weeks (200× magnification). (A color version of this figure is available in the online journal.)

lipid peroxidation. Whereas CAE staining also revealed inflammatory infiltrates with a peak at 12 weeks, no change of macrophage numbers was observed. Constant numbers of macrophages were already described by Leroux *et al*.[38] Even though their absolute number was unchanged, Kupffer cell phenotype might change to a more pro-inflammatory phenotype, which would lead to NAFLD progression.[39–42] The constant inflammatory

stimulus in this mouse model may be crucial for disease development. Noteworthy, not only the liver itself, but also adipose tissue inflammation,[43] circulating inflammatory cells, chemokines and cytokines, and the gut microbiota[44] have to be considered as potential sources of inflammation in NASH.[45]

The most striking observations were an impaired sinusoidal perfusion and reduced sinusoidal density, accompanied by a congested and irregular sinusoidal network with the sinusoids appearing to be quite tortuous with varying diameters. It is a well-known fact that sinusoidal congestion is increased in fatty livers with perfusion deficits arising simultaneously.[18,30,31,46,47] These disturbances might contribute to (especially macrovesicular) steatosis associated primary graft dysfunction, renal failure, requirement for retransplantation, and early biliary complications after transplantation.[48–50] Furthermore, it has been shown that changes in hepatic microcirculation contribute to impaired liver function in hepatic cirrhosis[51] and steatosis.[18,30] Recently, Schleicher *et al*.[52] constructed a mathematical model of lipid dynamics and oxygen paucity under HFD, and showed that development of steatosis is accompanied by swelling of hepatocytes, which reduces sinusoidal space and thus impairs hepatic microcirculation. Moreover, it was reported that blood velocity and volumetric blood flow are reduced in fatty livers[30] and inversely correlate with the degree of fat infiltration.[18] However, this could not clearly be observed in our study. In fact, in steatosis and steatohepatitis, it has been shown that sinusoids are compressed[30,31,45,53] due to swelling fatty hepatocytes. Consequently, sinusoids exhibit a smaller lumen. Even though we observed fat accumulation in hepatocytes and a lower sinusoidal density, sinusoids were not exclusively compressed but rather varied in diameter. Although we did not measure blood pressure in the liver, it might be possible that hypertension led to expansion of sinusoids particularly in end-stage liver disease. Similarly, Sun *et al*.[32] observed significantly wider hepatic cords and a reduced functional sinusoidal density in fatty rat livers, whereas no significant difference in sinusoidal diameter was noted. Macroscopic and microscopic observations of a, at least partially, highly vascularized liver surface and an increasing sinusoidal density indicate an angiogenic response in livers of 20 weeks old STZ/HFD-treated mice. This has previously been reported for fibrotic livers.[53] As also noticed via *in vivo* microscopy, changes in architecture of the sinusoidal network strongly correlate with disease severity. Thus, during progression of NAFLD, an irregular arrangement and distortion of sinusoids increased and was most prominent in end-stage liver disease (20 weeks). Furthermore, collagen deposition, which was observed throughout disease progression, leads to capillarization of sinusoids.[21,22] This further impairs nutritional and oxygen supply of the tissue [30,31,45,46,53] leading to increased ballooning and fibrotic remodeling of the liver.

Of importance, pathology of the here presented model does not exhibit all metabolic determinants of NAFLD, such as obesity and hyperinsulinemia. In fact, the mice are leaner than healthy animals and do not develop great amounts of fatty tissue, a commonly known problem of many NAFLD models. Through STZ-induced reduction of beta cell function, mice develop non-insulin-dependent diabetes mellitus. Even though the induced diabetes does not clearly reflect insulin resistance and hyperinsulinemia, it does mimic disturbed insulin signaling resulting in a net insulin deficiency on a cellular level. However, mice did not show absolute insulin deficiency, as also recently shown by Saito *et al*.[12] who suggested an existing insulin resistance in these mice. In most NAFLD patients, hyperinsulinemia and insulin resistance are the cause of hyperglycemia. A common issue of mouse models reflecting the metabolic syndrome more accurately is that progression of NAFLD occurs extremely slowly, with low incidence, or not at all.[8,9,54] Thus, these models are not suitable for studies using therapeutic intervention during NAFLD progression.

Interestingly, in the steatosis-inflammation-tumor model, liver tumors form without presence of cirrhosis or severe fibrosis. In humans, the formation of HCC can also be observed without development of fibrosis or cirrhosis.[2] Further analyses of tumorigenesis in the steatosis-inflammation-tumor mouse model might help to understand the underlying mechanisms of HCC formation without cirrhosis.

In conclusion, the steatosis-inflammation-tumor model is of high suitability for assessment of microcirculation in progressive NAFLD with underlying diabetes mellitus. The presence of characteristic microcirculatory disturbances at functional, morphological, and cellular level validates the suitability of this model to particularly investigate therapeutic approaches targeting leukocyte-endothelial interaction and sinusoidal perfusion.

Authors' contributions: BV and KA conceived the research ideas and supervised the project. ML and KA wrote and edited the manuscript. ML, AH, MK, and BG performed the experiments. AH, MK, BG, and BV reviewed and edited the manuscript. ML, AH, MK, BV, and KA analyzed the data.

ACKNOWLEDGMENTS

We thank Alexander Hartmann, Berit Blendow, Dorothea Frenz, Eva Lorbeer-Rehfeldt, Ilona Klammfuß, Mareike Degner, and Maren Nerowski for their excellent technical assistance. Furthermore, we thank Horst Nizze for the assistance in pathological appraisal of the histologies and Angela Kuhla for her good advice.

DECLARATION OF CONFLICTING INTERESTS

The author(s) declared no potential conflicts of interest with respect to the research, authorship, and/or publication of this article.

Funding

This work was supported by the Deutsche Forschungsgemeinschaft, Bonn-Bad Godesberg, Germany [AB 453/2-1].

REFERENCES

1. Dietrich P, Hellerbrand C. Non-alcoholic fatty liver disease, obesity and the metabolic syndrome. *Best Pract Res Clin Gastroenterol* 2014;**28**:637–53
2. Calzadilla LB, Adams L. The natural course of non-alcoholic fatty liver disease. *Int J Mol Sci* 2016;**17**:774.
3. World Health Organization. *Global health estimates 2015: deaths by cause, age, sex, by country and by region*, 2000–2015, Geneva.
4. White DL, Kanwal F, El-Serag HB. Non-alcoholic fatty liver disease and hepatocellular cancer: a systematic review. *Clin Gastroenterol Hepatol* 2012;**10**:1342–59
5. Day CP, James OF. Steatohepatitis: a tale of two 'hits'? *Gastroenterology* 1998;**114**:842–5
6. Tilg H, Moschen AR. Evolution of inflammation in nonalcoholic fatty liver disease: the multiple parallel hits hypothesis. *Hepatology* 2010;**52**:1836–46
7. Cortez-Pinto H, Camilo M, Baptista A, De Oliveira A, DE Moura M. Non-alcoholic fatty liver: another feature of the metabolic syndrome? *Clin Nutr* 1999;**18**:353–8
8. Nakagawa H. Recent advances in mouse models of obesity- and non-alcoholic steatohepatitis-associated hepatocarcinogenesis. *World J Hepatol* 2015;**7**:2110–8
9. Riordan JD, Nadeau JH. Modeling progressive non-alcoholic fatty liver disease in the laboratory mouse. *Mamm Genome* 2014;**25**:473–86
10. Heindryckx F, Colle I, Van Vlierberghe H. Experimental mouse models for hepatocellular carcinoma research. *Int J Exp Pathol* 2009;**90**:367–86
11. Fujii M, Shibazaki Y, Wakamatsu K, Honda Y, Kawauchi Y, Suzuki K, Arumugam S, Watanabe K, Ichida T, Asakura H, Yoneyama H. A murine model for non-alcoholic steatohepatitis showing evidence of association between diabetes and hepatocellular carcinoma. *Med Mol Morphol* 2013;**46**:141–52
12. Saito K, Uebanso T, Maekawa K, Ishikawa M, Taguchi R, Nammo T, Nishimaki-Mogami T, Udagawa H, Fujii M, Shibazaki Y, Yoneyama H, Yasuda K, Saito Y. Characterization of hepatic lipid profiles in a mouse model with nonalcoholic steatohepatitis and subsequent fibrosis. *Sci Rep* 2015;**5**: 12466
13. Jojima T, Tomotsune T, Iijima T, Akimoto K, Suzuki K, Aso Y. Empagliflozin (an SGLT2 inhibitor), alone or in combination with linagliptin (a DPP-4 inhibitor), prevents steatohepatitis in a novel mouse model of non-alcoholic steatohepatitis and diabetes. *Diabetol Metab Syndr* 2016;**8**:45
14. Ishikawa H, Takaki A, Tsuzaki R, Yasunaka T, Koike K, Shimomura Y, Seki H, Matsushita H, Miyake Y, Ikeda F, Shiraha H, Nouso K, Yamamoto K. L-carnitine prevents progression of non-alcoholic steatohepatitis in a mouse model with upregulation of mitochondrial pathway. *PLoS One* 2014; **9**: e100627.
15. Takaki Y, Saito Y, Takasugi A, Toshimitsu K, Yamada S, Muramatsu T, Kimura M, Sugiyama K, Suzuki H, Arai E, Ojima H, Kanai Y, Saito H. Silencing of microRNA-122 is an early event during hepatocarcinogenesis from non-alcoholic steatohepatitis. *Cancer Sci* 2014;**105**:1254–60
16. Konishi H, Shirabe K, Nakagawara H, Harimoto N, Yamashita YI, Ikegami T, Yoshizumi T, Soejima Y, Oda Y, Maehara Y. Suppression of silent information regulator 1 activity in noncancerous tissues of hepatocellular carcinoma: possible association with non-B non-C hepatitis pathogenesis. *Cancer Sci* 2015;**106**:542–9
17. Thomson JP, Ottaviano R, Unterberger EB, Lempiäinen H, Muller A, Terranova R, Illingworth RS, Webb S, Kerr a. RW, Lyall MJ, Drake a. J, Wolf CR, Moggs JG, Schwarz M, Meehan RR. Loss of Tet1-associated 5-hydroxymethylcytosine is concomitant with aberrant promoter hypermethylation in liver cancer. *Cancer Res* 2016;**76**:3097–08
18. Seifalian AM, Piasecki C, Agarwal A, Davidson BR. The effect of graded steatosis on flow in the hepatic parenchymal microcirculation. *Transplantation* 1999;**68**:780–4
19. Pasarín M, La Mura V, Gracia-Sancho J, García-Calderó H, Rodríguez-Vilarrupla A, García-Pagán JC, Bosch J, Abraldes JG. Sinusoidal endothelial dysfunction precedes inflammation and fibrosis in a model of NAFLD. *PLoS One* 2012;**7**:e32785
20. Rosenstengel S, Stoeppeler S, Bahde R, Spiegel H-U, Palmes D. Type of steatosis influences microcirculation and fibrogenesis in different rat strains. *J Investig Surg* 2011;**24**:273–82
21. DeLeve LD. Hepatic microvasculature in liver injury. *Semin Liver Dis* 2007;**27**:390–400
22. Vollmar B, Siegmund S, Menger MD. An intravital fluorescence microscopic study of hepatic microvascular and cellular derangements in developing cirrhosis in rats. *Hepatology* 1998;**27**:1544–53
23. Abshagen K, Eipel C, Menger MD, Vollmar B. Comprehensive analysis of the regenerating mouse liver: an in vivo fluorescence microscopic and immunohistological study. *J Surg Res* 2006;**134**:354–62
24. Eipel C, Eisold M, Schuett H, Vollmar B. Inhibition of heme oxygenase-1 protects against tissue injury in carbon tetrachloride exposed livers. *J Surg Res* 2007;**139**:113–20
25. Abshagen K, Eipel C, Kalff JC, Menger MD, Vollmar B. Kupffer cells are mandatory for adequate liver regeneration by mediating hyperperfusion via modulation of vasoactive proteins. *Microcirculation* 2007;**15**:37–47
26. Kleiner DE, Brunt EM, Van Natta M, Behling C, Contos MJ, Cummings OW, Ferrell LD, Liu YC, Torbenson MS, Unalp-Arida A, Yeh M, McCullough AJ, Sanyal AJ. Design and validation of a histological scoring system for nonalcoholic fatty liver disease. *Hepatology* 2005;**41**:1313–21
27. Abshagen K, Eipel C, Kalff JC, Menger MD, Vollmar B. Loss of NF-kappaB activation in Kupffer cell-depleted mice impairs liver regeneration after partial hepatectomy. *Am J Physiol Gastrointest Liver Physiol* 2007;**292**:G1570–7
28. Rahman R, Hammoud GM, Almashhrawi AA, Ahmed KT, Ibdah JA. Primary hepatocellular carcinoma and metabolic syndrome: an update. *World J Gastrointest Oncol* 2013;**5**:186–94
29. Farrell GC, Teoh NC and McCuskey RS. Hepatic microcirculation in fatty liver disease. *Anat Rec* 2008;**291**:684–92
30. Ijaz S, Yang W, Winslet MC, Seifalian a M. Impairment of hepatic microcirculation in fatty liver. *Microcirculation* 2003;**10**:447–56
31. McCuskey RS, Ito Y, Robertson GR, McCuskey MK, Perry M, Farrell GC. Hepatic microvascular dysfunction during evolution of dietary steatohepatitis in mice. *Hepatology* 2004;**40**:386–93
32. Sun CK, Zhang XY, Zimmermann A, Davis G, Wheatley AM. Effect of ischemia-reperfusion injury on the microcirculation of the steatotic liver of the Zucker rat. *Transplantation* 2001;**72**:1625–31
33. Tannapfel A, Denk H, Dienes HP, Langner C, Schirmacher P, Trauner M, Flott-Rahmel B. Histopathological diagnosis of non-alcoholic and alcoholic fatty liver disease. *Virchows Arch* 2011;**458**:511–23
34. Xia J, Yuan J, Xin L, Zhang Y, Kong S, Chen Y, Yang S, Li K. Transcriptome analysis on the inflammatory cell infiltration of nonalcoholic steatohepatitis in Bama minipigs induced by a long-term high-fat, high-sucrose diet. *PLoS One* 2014;**9**:1–22
35. Kowalewska PM, Patrick AL, Fox-Robichaud AE. Innate immunity of the liver microcirculation. *Cell Tissue Res* 2011;**343**:85–96
36. Collins T, Read MA, Neish AS, Whitley MZ, Thanos D, Maniatis T. Transcriptional regulation of endothelial cell adhesion molecules: NF-kappa B and cytokine-inducible enhancers. *FASEB J* 1995;**9**:899–909
37. Wang T, Zhang X, Li JJ. The role of NF-kappaB in the regulation of cell stress responses. *Int Immunopharmacol* 2002;**2**:1509–20
38. Leroux A, Ferrere G, Godie V, Cailleux F, Renoud ML, Gaudin F, Naveau S, Prévot S, Makhzami S, Perlemuter G, Cassard-Doulcier AM. Toxic lipids stored by Kupffer cells correlates with their pro-inflammatory phenotype at an early stage of steatohepatitis. *J Hepatol* 2012;**57**:141–9
39. Reid DT, Reyes JL, McDonald B a., Vo T, Reimer R a., Eksteen B. Kupffer cells undergo fundamental changes during the development of experimental nash and are critical in initiating liver damage and inflammation. *PLoS One* 2016;**11**:e0159524
40. Maina V, Sutti S, Locatelli I, Vidali M, Mombello C, Bozzola C, Albano E. Bias in macrophage activation pattern influences non-alcoholic steatohepatitis (NASH) in mice. *Clin Sci* 2012;**122**:545–53
41. Sakaguchi S, Takahashi S, Sasaki T, Kumagai T, Nagata K. Progression of alcoholic and non-alcoholic steatohepatitis: common metabolic

aspects of innate immune system and oxidative stress. *Drug Metab Pharmacokinet* 2011;**26**:30–46
42. Wan J, Benkdane M, Teixeira-Clerc F, Bonnafous S, Louvet A, Lafdil F, Pecker F, Tran A, Gual P, Mallat A, Lotersztajn S, Pavoine C. M2 Kupffer cells promote M1 Kupffer cell apoptosis: a protective mechanism against alcoholic and nonalcoholic fatty liver disease. *Hepatology* 2014;**59**:130–42
43. Cusi K. Role of obesity and lipotoxicity in the development of non-alcoholic steatohepatitis: pathophysiology and clinical implications. *Gastroenterology* 2012;**142**:711–25
44. Wigg a J, Roberts-Thomson IC, Dymock RB, McCarthy PJ, Grose RH, Cummins a G. The role of small intestinal bacterial overgrowth, intestinal permeability, endotoxaemia, and tumour necrosis factor alpha in the pathogenesis of non-alcoholic steatohepatitis. *Gut* 2001;**48**:206–11
45. Farrell GC, Van Rooyen D, Gan L, Chitturi S. NASH is an inflammatory disorder: Pathogenic, prognostic and therapeutic implications. *Gut Liver* 2012;**6**:149–71
46. Seifalian AM, Chidambaram V, Rolles K, Davidson BR. In vivo demonstration of impaired microcirculation in steatotic human liver grafts. *Liver Transpl Surg* 1998;**4**:71–7
47. Teramoto K, Bowers JL, Kruskal JB, Clouse ME. hepatic microcirculatory changes after reperfusion in fatty and normal liver transplantation in the rat. *Transplantation* 1993;**56**:1076–82
48. de Graaf EL, Kench J, Dilworth P, Shackel NA, Strasser SI, Joseph D, Pleass H, Crawford M, Mccaughan GW, Verran DJ. Grade of deceased donor liver macrovesicular steatosis impacts graft and recipient outcomes more than the Donor Risk Index. *J Gastroenterol Hepatol* 2012;**27**:540–6
49. McCormack L, Petrowsky H, Jochum W, Mullhaupt B, Weber M, Clavien P-A. Use of severely steatotic grafts in liver transplantation: a matched case-control study. *Ann Surg* 2007;**246**:940–8
50. Spitzer AL, Lao OB, Dick AAS, Bakthavatsalam R, Halldorson JB, Yeh MM, Upton MP, Reyes JD, Perkins JD. The biopsied donor liver: incorporating macrosteatosis into high-risk donor assessment. *Liver Transplant* 2010;**16**:874–84
51. Villeneuve JP, Dagenais M, Huet PM, Rov A, Lapointe R, Marleau D. The hepatic microcirculation in the isolated perfused human liver. *Hepatology* 1996;**23**:24–31
52. Schleicher J, Guthke R, Dahmen U, Dirsch O, Holzhuetter HG, Schuster S. A theoretical study of lipid accumulation in the liver-implications for nonalcoholic fatty liver disease. *BBA Mol Cell Biol Lipids* 2014;**1841**:62–9
53. Vanheule E, Geerts AM, Van Huysse J, Schelfhout D, Praet M, Van Vlierberghe H, De Vos M, Colle I. An intravital microscopic study of the hepatic microcirculation in cirrhotic mice models: relationship between fibrosis and angiogenesis. *Int J Exp Pathol* 2008;**89**:419–32
54. Anstee QM, Goldin RD. Mouse models in non-alcoholic fatty liver disease and steatohepatitis research. *Int J Exp Pathol* 2006;**87**:1–16

(Received July 19, 2017, Accepted October 3, 2017)